

Formation of Nanooctahedra in Molybdenum Disulfide and Molybdenum Diselenide Using Pulsed Laser Vaporization

Philip A. Parilla,^{*,†} Anne C. Dillon,[†] Bruce A. Parkinson,[‡] Kim M. Jones,[†] Jeff Alleman,[†] Gerald Riker,[†] David S. Ginley,[†] and Michael J. Heben[†]

National Renewable Energy Laboratory, Golden, Colorado 80401, and
Chemistry Department, Colorado State University, Fort Collins, Colorado 80523

Received: July 28, 2003; In Final Form: March 1, 2004

Pulsed laser vaporization has been used to produce nanooctahedra of MoS₂ and MoSe₂. The nanooctahedra primarily form in two- or three-layer nested octahedra, although nesting up to five layers has been observed. Tilting the TEM sample stage and mapping how the images of single particles transformed provided the evidence to verify their octahedral geometry. Analysis of 30 two- and three-layered octahedra showed that their outer edge lengths clustered at ~3.8 nm and ~5.1 nm, respectively. This discreet sizing and the high symmetry of these closed nanooctahedra represent the closest inorganic analogy yet to the carbon fullerenes. The geometrical implications for forming octahedra from these layered compounds are investigated by considering different atomic arrangements assuming either trigonal prismatic or octahedral coordination around the Mo atom and yields two possible configurations for the actual structure of the nanooctahedra. A preliminary survey of pulsed laser vaporization of other layered metal chalcogenides shows that these dichalcogenides differ in their tendency to form small closed layered fullerene-like structures. These materials can be ranked from highest tendency to lowest as follows: NbSe₂, WS₂, WSe₂, SnS₂, TaS₂, GaS, ReS₂, and MoTe₂.

Introduction

The discovery of carbon fullerenes¹ and nanotubes² has led to a vast research area generating interesting science and new technologies.^{3–5} It also has led to the natural question of whether analogous structures can be found in inorganic materials. The term “fullerene” applies to caged carbon structures formed by the seamless integration of graphite fragments. Closure is favored when the total energy lowered by dangling bond elimination outweighs the energy costs of curvature-induced strain and bonding defects necessary for closure. The smallest cages are stable when strain energy is adequately distributed by a highly symmetric structure that also satisfies bonding requirements. This last concept is the defining characteristic of a “true” fullerene, such as C₆₀. Initial studies to investigate fullerene-like structures in layered inorganic materials such as BN and MX₂ (M=Mo, W; X=S, Se) resulted in the discovery of nested polyhedra and nanotubes.^{6–9} These discoveries proved that inorganic materials could form closed layered structures analogous to the larger fullerenes such as “bucky onions” and multiwall carbon nanotubes.

The conditions needed to produce smaller closed structures are distinctly different than those to produce large ones. The smaller structures represent a local minimum in the free energy of formation within a restricted configuration space. Specifically, they form under conditions where the local number of atoms remains small and the energy of the constituents is large enough to allow adequate sampling of structural conformations to reach the local minimum. Furthermore, once this minimum has been found, the energy should be removed from the structure to prevent a larger, more stable structure from forming with the eventual encounter with more material. This description exactly

matches the conditions used to form Buckminsterfullerene.¹ Recently, the search for inorganic fullerene-like materials has continued by examining more energetic synthetic techniques^{10–13} and other layered materials.^{10,14–16} The analogy with carbon, however, is not complete since caged structures with discreet sizes and shapes appear to be rare and, only recently, have been demonstrated outside of the carbon family.^{13,17,18} Similar to the carbon fullerenes, closed inorganic cages should be highly symmetric and occur in specific sizes with discreet increases in the number of atoms from one size to the next.

The transition-metal dichalcogenides, MX₂, where M is a transition metal and X, a chalcogen, have been investigated for fullerene-like behavior due to their tendency to form layered structures. A single layer consists of a strongly bound X–M–X sandwich that is weakly stacked with other layers. The crystal structures vary in the number of layers per unit cell and how the layers are aligned with respect to one another.¹⁹ Thus, the layered transition-metal dichalcogenides are excellent analogues to graphite. Another important and distinguishing characteristic for these compounds is the bonding coordination of the metal. Primarily, this occurs in one of two variants, either trigonal prismatic or octahedral coordination. The octahedral coordination can be further subclassified as being distorted (usually with metal–metal bonding) or undistorted. As an example, Figure 1a shows the unit cell of MoS₂ in its most common molybdenite form (2H–MoS₂, *P6₃/mmc*). The Mo atoms form a layer that is sandwiched above and below by S layers and form a trilayer sheet (Figure 1b). Within each layer of the trilayer, the atoms reside on a trigonal lattice and are aligned with respect to each other, resulting in trigonal prismatic bonding coordination for the metal (Figure 1c). In contrast, exfoliated MoS₂ has octahedral metal bonding coordination (1T–MoS₂) as shown in Figure 1d.²⁰ The two coordinations are very similar to each other, and one can be obtained from the other by rotating the upper three atoms with respect to the lower three atoms by 60 degrees in the plane.

* Corresponding author. E-mail: philip_parilla@nrel.gov

[†] National Renewable Energy Laboratory.

[‡] Colorado State University.

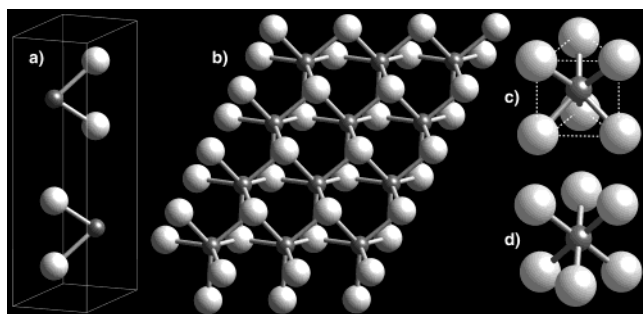


Figure 1. (a) The unit cell for 2H-MoS₂ shows that each Mo (small dark sphere) layer has a S (large light sphere) layer above and below it to form a trilayer sandwich. There are two trilayers per unit cell in 2H-MoS₂. (b) A single trilayer sheet showing trigonal prismatic coordination around the Mo atom. The S atoms have trigonal pyramidal bonding with the Mo. (c) Trigonal prismatic coordination found in bulk 2H-MoS₂. (d) Octahedral coordination for 1T-MoS₂ found in exfoliated samples.

In its most common form, molybdenum diselenide, MoSe₂, is isostructural with 2H-MoS₂. Both of these materials, as well as other layered metal chalcogenides, are used in this investigation of the formation of fullerene-like materials.

This report provides the details of producing highly symmetric two- and three-layer nanooctahedra of MoS₂ and MoSe₂ by pulsed laser vaporization and the evidence supporting their octahedral structure. These nanooctahedra may be the first true “inorganic fullerenes” (IFs).¹³ Additionally, we report on the initial investigations of other layered chalcogenide compounds for evidence of inorganic fullerene structures; many of these show promising indicators and deserve further investigation.

Experimental Section

MoS₂ targets were prepared by pressing 5 g of 98+% MoS₂ powder (Aldrich and Alfa) in a 28.8 mm dye at room temperature for 5 min at 10 metric tons. The targets were positioned in a 1.5 in. diameter quartz tube enclosed in a clamshell single-zone furnace. The tube was evacuated to ~2 Torr and backfilled with helium or argon twice before pressures of 500 to 800 Torr were established with a constant gas flow rate of ~90 sccm. Light from a Lambda Physik EMG-50E KrF excimer laser (248 nm) with an energy fluence of ~10 J/cm² (~300 mJ/pulse, ~20 ns pulse width) was directed through a window and down the tube to the target. Pulsed laser vaporization (PLV) occurred with 8 Hz pulses while the beam was manually rastered to a new position on the target every 4 min for a total of 20 min. Black soot deposits formed on the tube both in front of and behind the target. A series of experiments with the chamber/target temperature ranging between 30 and 600 °C were performed.

A second PLV system using a Nd:YAG laser allowed better control of the experimental parameters. Improvements included better vacuum and gas flow capabilities and the introduction of an automatic laser beam raster. Target preparation followed the same procedure as the excimer laser experiments. After placing the target in the 2 in. diameter quartz tube, it was evacuated to ~20 mTorr and backfilled with argon to pressures ranging from 20 to 1000 Torr under a flow of ~100 sccm. The Nd:YAG laser for this system has both long-pulse and Q-switched modes as well as a higher energy output up to 1 J/pulse. Experiments were performed at 10 Hz with the long pulse mode and average powers ranging from 4 to 6 W. The beam was continuously rastered over the target at a rate of ~2 mm/s. The runs lasted for 1000 s to 10,000 s and were nominal at room temperature.

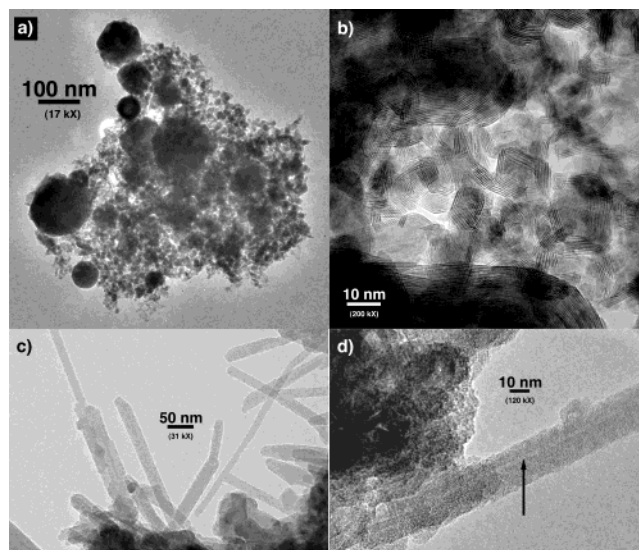


Figure 2. Typical TEM images of the different types of structures found in the soot collected from laser vaporization of MoS₂. Structures include (a) roughly spherical particles, (b) a variety of nested polyhedra, and (c) tubes with diameters ranging between 15 and 35 nm. The image in (d) shows a tube that is asymmetrically coated with amorphous material and the hollow interior is clearly visible (arrow).

The Nd:YAG PLV system was used to investigate several other layered chalcogenide compounds for evidence of inorganic fullerenes and fullerene-like structures. Examined materials included MoSe₂, MoTe₂, WS₂, WSe₂, SnS₂, GaS, TaS₂, NbSe₂, and ReS₂. Target preparation proceeded similarly as above, using the respective bulk powders with the exception of SnS₂ and GaS, where large single crystals grown via a Bridgman technique were used. The laser vaporization was performed under 200 Torr of argon and with other conditions as stated above.

Transmission electron microscopy (TEM) examination of the samples was done using a Philips CM-30 microscope operating at 200 kV. Samples were prepared by dispersing a fraction of the soot collected from the reactor wall in acetone or methanol by mild ultrasonication, and then placing a few drops onto a 200-mesh lacy carbon grid. X-ray diffraction (XRD) $\theta/2\theta$ measurements were used to determine the crystalline phase composition of the laser-generated soot. The diffractometer is a Scintag PTS 4-circle goniometer with a Cu K α anode source operating at 45 kV/40 mA and a solid-state LN₂-cooled Ge X-ray detector coupled to a single channel analyzer. Raman spectroscopy was performed using ~7 mW of the 488 nm line of an Ar ion laser with a resolution of 2–4 cm⁻¹. The scattered light was analyzed with a Jobin Yvon 270M spectrometer with a 2400 grooves/mm grating equipped with a liquid-nitrogen-cooled Spectrum One CCD and a holographic notch filter. A Nikon 55 mm camera lens was employed both to focus the beam on the sample to a ~0.25 mm² spot and to collect the Raman scattered light.

Results and Discussion

Synthesis. Material collected from the initial experiments using the excimer laser MoS₂ targets and performed at temperatures between 30 and 500 °C contained crystalline and amorphous fractions as observed by TEM. The XRD data of the soot identified four crystalline phases (Mo, S, MoS₂, and a small amount of Mo₂S₃) with no unidentified peaks. The crystalline material included large sheets, roughly spherical particles (Figure 2a) and a variety of nested polyhedra (Figure

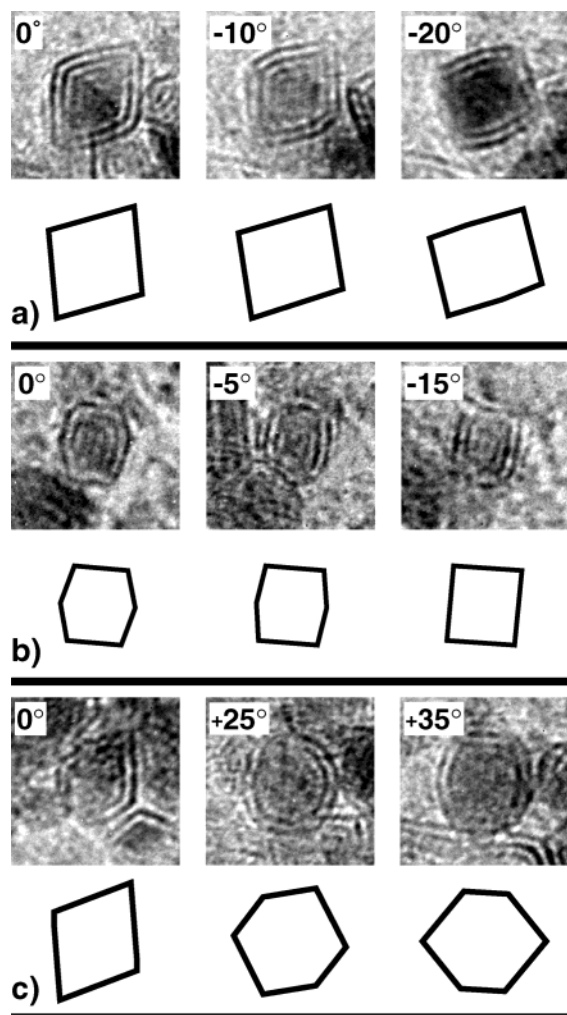


Figure 3. TEM images of MoS_2 structures undergoing transformation during TEM stage tilting. (a), (b), and (c) each track different particles through the tilting experiments. The relative rotation angle is the number in the upper left corner of each image. The dimension of each image height and width is 10 nm. The stick figures below each image are the predicted projection outline calculated from an ideal octahedron undergoing an identical rotation (see text).

2b) and tubes (Figure 2c and 2d) with diameters ranging between 15 and 35 nm. The nested polyhedra are quite similar to those previously reported following the gas-phase reaction between MoO_{3-x} and H_2S at elevated temperatures.²¹ Closer examination of the soot revealed a population of smaller rhomboidal, hexagonal, and rectangular TEM projections (Figures 3a left, 3b left, and 3b right, respectively) approximately 3–5 nm in size and having two or three layers. A few four- or five-layer structures with these geometries were observed, but not in quantities sufficient to allow their systematic study. Qualitatively, the density of these structures compared to the densities of the other components did not change significantly for syntheses performed at or below 500 °C. In contrast, TEM analyses of soot produced at temperatures of 550 °C and above revealed predominately crystalline folded sheets of MoS_2 with no smaller rhomboidal, rectangular, and hexagonal TEM projections observed.

The effects of inert gas pressure on the synthesis were performed in the Nd:YAG PLV system. At pressures between 200 and 800 Torr, the material produced by the Nd:YAG laser showed no qualitative difference to that from the excimer laser; however, only ambient (room) temperature runs have been performed with the Nd:YAG system. At 20 Torr, the yield of

soot material drastically decreased and a film-like coating on the reactor walls was obtained instead. For runs at 1000 Torr, almost no soot accumulated onto the reactor wall and rhomboidal, rectangular, and hexagonal structures were not found in TEM images.

TEM Analysis. The small rhomboidal, rectangular, and hexagonal structures were investigated for closure with TEM tilting studies. Many individual two- and three-layer structures were tilted with respect to the incident electron beam, and images were collected at various angles. The first image in the series of Figure 3a shows a closed three-layer rhomboidal projection. Tilting the stage -10° produced a projection with an increased acute angle and a decreased obtuse angle. Further tilting for a total angular displacement of -20° resulted in a projection that is nearly rectangular. Similar behavior is seen in Figure 3b, where a 2-layer hexagonal image is transformed into a more rectangular shape, and in Figure 3c displaying the transformation of another 2-layer hexagon into a rhombus. The data in Figure 3 and similar data from over 30 different 2- and 3-layered structures clearly demonstrate that these structures are closed.

The types of transformations observed during tilting are all consistent with a three-dimensional (3D) octahedron producing the two-dimensional (2D) projections observed in TEM. The faces of an octahedron are equilateral triangles that share the symmetry of the trigonal Mo and S sublattices in MoS_2 . For projections with edges aligned approximately parallel to the beam, the TEM images show evidence of substantial rounding at these edges. In contrast, projected images of the vertices appear relatively sharp; an example of both of these situations is shown in Figure 4a. Although the exact structure of the MoS_2 octahedron's six vertices presently is unclear, one might expect either a four-member Mo ring^{9,22} or a single Mo atom to be stable. Figure 4b illustrates a possible Mo trigonal sublattice for these nanooctahedra with the vertices shown as four-member rings.

Computer Modeling. The relationship between a 3D octahedron and its 2D projections found in TEM imaging was explored by mathematical modeling where an ideal octahedron was systematically oriented in 3D and projected onto the $z = 0$ plane. Its orientation was defined using the Euler angle convention (ϕ, θ, ψ) around the fixed $z-x-z$ axes.²³ The inherent symmetry of the octahedron ensured that all possible projections could be generated with only ϕ and θ rotations, both between 0 and 90° . Variations in ψ only changed the orientation of the 2D projection in the $z = 0$ plane and not the shape of the projection. The survey was performed in 0.2° increments of ϕ and θ , and the results were tabulated. The most striking feature of this survey is that the projection space can be broken into two regions: 4-sided and 6-sided projections (see Figure 5). The approximate areal percentages for these two regions are 72% and 28% for the 4-sided and 6-sided regions, respectively. Experimentally, classification of the TEM projections into 4- or 6-sided shapes does not yield similar percentages, with 6-sided projections occurring rarely ($\sim 7\%$ of the projections). There are a number of possible explanations for this result. One of these is that much of the 6-sided region consists of projections that have two vertices with angles approaching 180° , thereby making it hard to distinguish from a 4-sided projection. This is further exacerbated by the additional ambiguity introduced by rounded edges. Another distinct possibility is a nonuniform distribution of nanooctahedra orientations on the TEM grid.

The black bars in Figure 6 show the frequency distribution as a function of the vertex angle for all 4-sided 2D projections

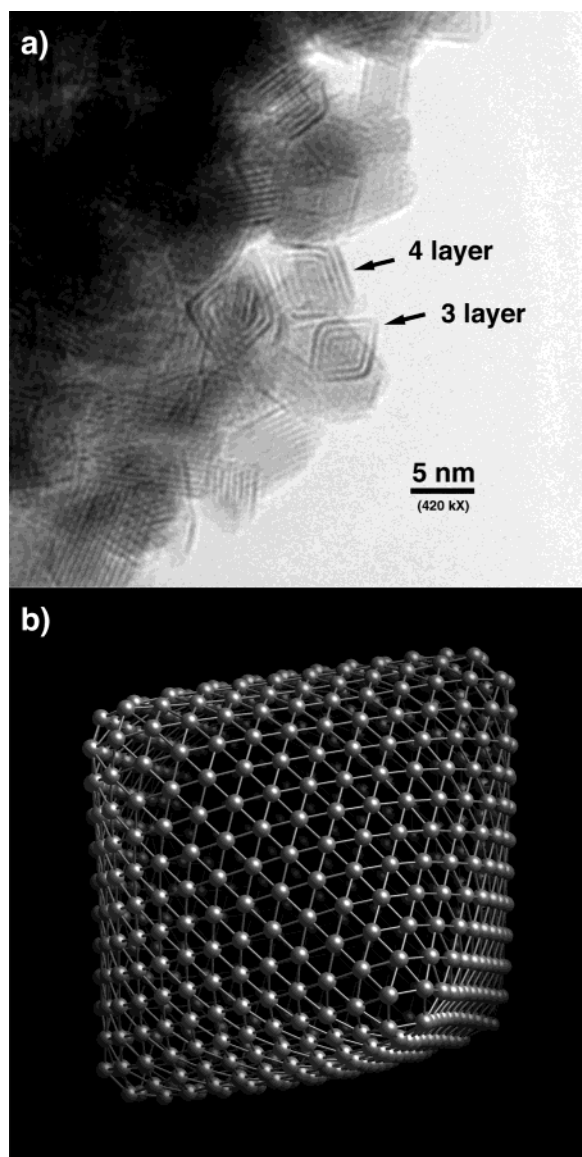


Figure 4. (a) TEM image of a three-layered nanooctahedron produced from vaporization using a Nd:YAG laser. The octahedron is oriented to produce a rhomboidal projection from the electron beam. Notice the visible rounding observed at the edges (obtuse angles) while faint but sharp vertices (acute angles) are also observed. Additionally, there is a candidate four-layer nanooctahedron partially obscured and situated near the three-layer one. (b) Model of an idealized Mo trigonal sublattice in a nanooctahedron.

that can be produced by an ideal octahedron. The sharp peak at 90° shows that square and rectangular projections are encountered most often while stepping through the ϕ - θ space. Figure 6 also shows a histogram of the measured angles (gray bars, error $\sim \pm 4^\circ$) formed by the sides of 28 unique untitled four-sided MoS_2 layered structures found during TEM analysis and similar to those in Figure 3. Even though the measured histogram is only weakly peaked at 90° , it should be noted that all angles, within error, fall in the allowed range (71° – 109°) for four-sided projections of an octahedron. The fact that the histogram of measured angles differs from the calculated trace also suggests that the MoS_2 octahedra may prefer specific orientations on the TEM grid. For example, almost all of the soot material has substantial van der Waals surfaces that tend to agglomerate to each other and to the TEM grid. For the nanooctahedra, the facets will be the van der Waals surface that binds it to the other material. Furthermore, most of the

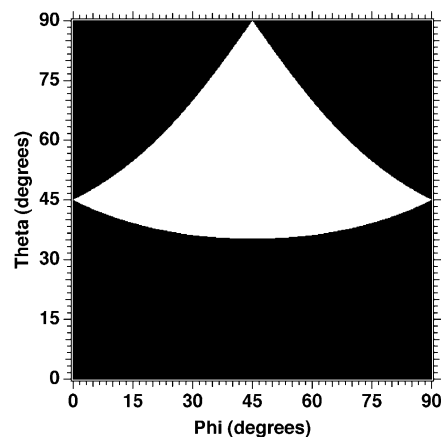


Figure 5. Mapping of how the projections of an octahedron can be either four-sided (parallelogram, black area) or six-sided (hexagon, white area). The axes represent rotations according to the Euler convention (ϕ, θ, ψ) around the fixed z - x - z axes. Only ϕ and θ rotations, both between 0° and 90° , are needed to completely survey the types of projections produced.

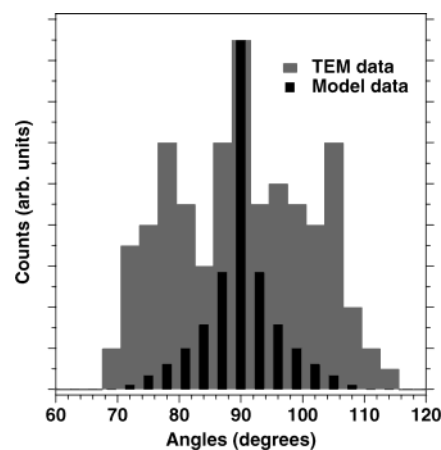


Figure 6. Histograms comparing model-generated data (black bars) with the TEM-measured (gray bars) vertex angles for four-sided projections. Within error, the experimentally measured angles fall entirely within the expected range for octahedron projections (71° – 109°).

nanooctahedra were observed near the periphery of agglomerated materials, as required for optimal TEM imaging. These tendencies are sufficient to influence the frequency distribution of the vertex angles and cause the nanooctahedra to not assume all orientations with equal probability.

Similar methods were used to analytically model the TEM tilt experiments. In this simulation, the TEM rotation axis was the only degree of freedom and was constant for all rotations at a given magnification. One image in a rotation series set the Eulerian angles and defined the rotation origin. All other projection shapes could then, in principle, be predicted in a given tilt series. The stick figures directly beneath the TEM images of Figure 3 are the simulated 2D projections of an octahedron for an identical TEM tilt. The agreement is almost exact in Figures 3a and 3b, giving strong support for the closed 3D structure and the existence of MoS_2 regular octahedra. Not all tilting experiments could be readily modeled, and Figure 3c displays one such sequence. Slight movements of the particles on the TEM grid during rotation of the stage or perturbations by the electron beam are plausible explanations for the observed discrepancy between experiment and modeling. However, it should be emphasized that any individual image can still be represented by a projection of an octahedron.

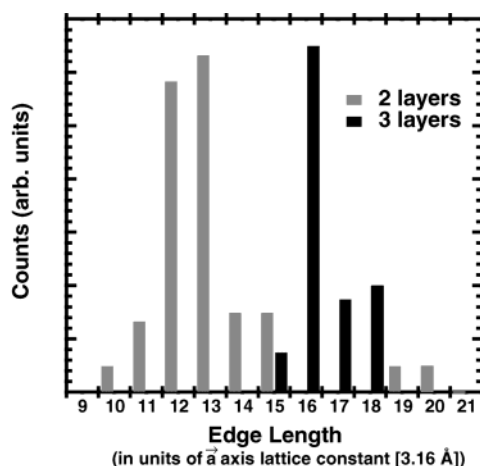


Figure 7. Histogram of MoS₂ octahedron edge lengths calculated from the TEM images. Lengths are in units of the a lattice constant (3.16 Å). The contributions from two- and three-layered structures are shaded differently for clarity. Two pronounced peaks at 12–13 and 16 lattice constants are associated with the two- and three-layer species, respectively, and imply that the octahedra tend to form in discreet sizes.

Nanooctahedra Edge Lengths. Our evidence clearly supports a regular octahedral structure, and with this supposition, the octahedral edge length may be calculated from the TEM projections. In particular, with the coordinate-system origin at the octahedron's geometric center, the vectors describing the location of the vertices all have equal magnitudes and adjacent vectors are mutually perpendicular. Using these facts, one can solve for the vector's magnitude from orthogonal pairs of the projected vertices in the TEM images and the resulting edge length is simply $\sqrt{2}$ times this magnitude. Figure 7 is a histogram of the edge lengths (in units of bulk MoS₂ a lattice constant, 3.16 Å) derived from 30 two- and three-layer rhomboidal, rectangular, or hexagonal TEM projections from samples produced via the excimer laser. A four-sided projection with its four projected vertices has four unique orthogonal pairs and yields four estimates of the edge length; each of these contributes 1/4 of a count to the histogram. Correspondingly, a six-sided projection with its six projected vertices has twelve unique orthogonal pairs and yields twelve estimates for the edge length; each of these contributes 1/12 of a count to the histogram. The error associated with assigning a given measurement to a histogram bin is estimated to be ± 0.5 bins. Two pronounced peaks at 12–13 and 16 lattice constants are associated with the two- and three-layer species, respectively, and imply that the octahedra form in discreet sizes. This is significant since the original class of inorganic fullerene-like materials has shown no indication of discreet sizes.⁹ The nanooctahedra thus represent a new class of inorganic fullerenes where both high symmetry and discreet sizes are defining characteristics similar to the family of carbon fullerenes.

The discreet sizes observed here are a subset of all the possible sizes for these nanooctahedra. The reason this subset predominates is unknown at this time. It is possible that this predominance is an artifact of our production process that may favor formation of this particular subset. More likely, however, is that underlying stability issues exist for the nanooctahedra that would hinder or preclude formation of certain sizes. For example, smaller nanooctahedra have a much higher concentration of strain since there are fewer atoms to distribute any strain inherent to this closed structure. This high strain may make the structure unstable, allowing disintegration or transformations to a larger octahedron. The observed nanooctahedra may represent the minimum size that is reasonably stable with respect

to the production process. Additional nested layers would then produce a discreet size series determined by the nesting geometry. These same stability issues may also explain why no single-layer nanooctahedra are observed. Perhaps the van der Waals bonding between nested octahedra provides an additional degree of stability needed for these structures to exist. The results of a recent calculation for metal chalcogenide nanotubes support this concept. Seifert et al.²⁴ found that among small planar sheets (multilayer or single-layer) and nanotubes (also multilayer or single-layer), only the sheets and multiwalled nanotubes are sufficiently stable to be observed. They found that there existed a critical value in the number of atoms, above which multiwall nanotubes are the lowest energy configuration and below which, specific planar sheet configurations have the lowest energy. This calculation can explain why no single-walled metal chalcogenide nanotube has ever been observed.²⁴

For ideal nested octahedra, there is a simple geometric relation linking the difference in edge lengths of two adjacent layers to the interplanar distance of the faces. This relation is

$$\frac{\Delta c}{a} = \frac{\Delta N}{\sqrt{6}} \quad (1)$$

where Δc is the interplanar distance (for example, Mo plane to Mo plane) and ΔN is the difference in edge lengths of the nested Mo layers in units of the a lattice constant. For bulk 2H-MoS₂, the $\Delta c/a$ ratio is 1.945 and implies ΔN should be 4.76. Since the edge lengths in units of a must be integers, their difference, ΔN , also must be an integer, thereby suggesting ΔN is 4 or, more likely, 5 if the bulk $\Delta c/a$ ratio is to be approximately maintained. The histogram of Figure 7 suggests that ΔN is 3 or 4 and implies a $\Delta c/a$ ratio less than the bulk. Direct measurements of the spacing between the nested octahedra observed by TEM yield 6.2 ± 0.6 Å, in good agreement with the layer spacing in bulk MoS₂ (6.15 Å = $c/2$). This TEM value together with the histogram result suggest that the a lattice constant in the nanooctahedra is larger than the bulk value; however, given the uncertainty in the measurement, this remains an open question. Interestingly, the type of metal bonding coordination is relevant to this question.

Bonding Coordination. Both trigonal prismatic and octahedral metal bonding coordinations occur in MoS₂ for the bulk and exfoliated forms, respectively, and so we consider that either may occur in the nanooctahedra. Both types of metal–chalcogenide bonding are common for the general family of transition metal dichalcogenides.¹⁹ That the energy difference between the trigonal prismatic and octahedral coordinations can be small is demonstrated by TaS₂ and TaSe₂ having both polytypes as well as a polytype with alternating layers of each coordination.^{19,25} The energy difference at STP between the octahedral and trigonal prismatic coordinations for TaSe₂ is approximately 4 kcal/mol.²⁵ Comparing this with the heat of formation (~ -61 kcal/mol²⁶) reveals only a 7% difference in the energies. The octahedral coordination of exfoliated MoS₂²⁰ suggests that the energy difference between the trigonal prismatic and octahedral forms of MoS₂ is small.²⁷ In addition, the high temperature form of MoTe₂ (β -MoTe₂) has distorted octahedral metal coordination with metal–metal bonding while the low-temperature phase (α -MoTe₂) has trigonal prismatic coordination, demonstrating that the stable bonding geometry can differ with temperature.¹⁹

There is currently no definitive evidence to support either the trigonal prismatic or the octahedral coordination in the nanooctahedra. An argument for octahedral coordination is the evidence for a larger a lattice constant discussed previously.

For a constant metal–chalcogenide bond length, it is expected that the a lattice constant in an ideal octahedral coordination will be 8% larger than that in the ideal trigonal prismatic coordination.¹⁹ In fact, the $\Delta c/a$ ratio in eq 1 for ideal octahedral coordination is 1.633, which then predicts $\Delta n = 4$, in excellent agreement with the data of Figure 7. However, the $\Delta c/a$ bulk value for MoS₂ must be reduced by 16% to achieve this agreement. There has also been a recent calculation that shows the a lattice constant increases in MoS₂ nanotubes with trigonal prismatic coordination.²² They found that the “in-plane” Mo–Mo distance increased by $\sim 8\%$ over the bulk value due to an increase in the Mo–S bond lengths for these curved structures. Perhaps a similar calculation using octahedral coordination would also yield a comparable a -lattice expansion, and the two effects together, conversion to octahedral coordination and increased Mo–S bond lengths in curved nanostructures, could provide the a -lattice expansion needed to agree with the data.

Raman spectroscopy can be used to determine the bonding coordination under the proper conditions. This was previously done for exfoliated MoS₂ where the Raman spectra were measured and the expected Raman signatures were calculated for single-layer MoS₂ sheets with either the trigonal prismatic or octahedral coordination.^{20,28} Specifically, trigonal prismatic coordination exhibits three Raman modes corresponding to E'', E', and A₁' at 287 cm⁻¹, 383 cm⁻¹, and 409 cm⁻¹ respectively. For octahedral coordination, there are two modes, E_{1g} and A_{1g}, at 290 cm⁻¹ and 413 cm⁻¹, respectively. Thus, the signature for the octahedral coordination is the absence of a signal near 383 cm⁻¹ in conjunction with the presence of signals near 290 cm⁻¹ and 413 cm⁻¹. For the exfoliated MoS₂, additional peaks also appeared at 156 cm⁻¹, 226 cm⁻¹, and 333 cm⁻¹ and were associated with the existence of a superlattice, thereby bringing new Raman modes into the Brillouin zone center.²⁸ While these new modes are not directly associated with octahedral coordination, they probably indicate a stronger metal–metal interaction that octahedral coordination may allow. The Raman data for the MoS₂ soot produced here showed peaks consistent with bulk MoS₂ and sulfur, in agreement with the XRD data that indicated both of these materials were present in the soot. Thus the mode near 383 cm⁻¹ was present but it cannot be ascribed to originating solely from the nanooctahedra since the soot contained the bulk material as well. There were no indications in the Raman data for the modes associated with the superlattice. The information obtained from Raman experiments will become more definitive once purified nanooctahedra samples become available.

Atomic Positions, Stoichiometry, and Bonding Saturation.

There are geometrical implications for the positions of the atoms, stoichiometry, and bond saturation in forming an octahedron out of a trilayer material such as MoS₂. For example, the atoms of the inside sulfur layer will be more crowded than the outside layer if the number of sulfur atoms in these two layers are equal. This is especially true near the edges of the octahedron where the trilayer bends and compresses/expands the inner/outer sulfur layers, respectively. The resulting strain energy will be minimized by distributing the strain over a wider area and accounts for the rounding of these edges as observed in the TEM data. For the discussion here, we present a geometrical analysis for placing sulfur atoms above and below a Mo sublattice shaped into an octahedron. Both trigonal prismatic and octahedral molybdenum coordinations to the sulfur are considered. We do not consider atomic reconstructions such as metal–metal bonding (found in high-temperature polytypes of MoTe₂ and WTe₂) or other possible defects that may relieve strain in the

closed structure. Rather, we consider an idealized MoS₂ octahedron and show that different configurations for the sulfur atoms can lead to deviations in stoichiometry, over-saturated and under-saturated bonding, and atomic crowding. There also exist two configurations in which these problems are mostly eliminated and therefore represent promising candidates for the actual structure of the nanooctahedra. Altogether we examine six configurations.

There are four configurations where all eight faces of the octahedron are equivalent; this produces MoS₂ nanooctahedra with full octahedral group symmetry (O_h). These four configurations are obtained by placing the S atoms above and below a Mo sublattice in all the possible permutations. Two have trigonal prismatic coordination and two have octahedral coordination about the molybdenum. Figure 8a illustrates this principle with a representation of two adjacent octahedron faces with a superimposed trigonal lattice and sites labeled 'A', 'B', and 'C'. The Mo atoms are sandwiched between the S layers and must lie on the sites labeled 'A' which include edge and vertex sites of the octahedron; if the Mo atoms were not on the 'A' sites, there would be significant deviations from ideal MoS₂ stoichiometry for the O_h configurations. The S atoms will lie above and below the sites labeled 'B' or 'C'. If the upper and lower sulfur atoms are both on 'B' (BAB, Figure 8b) or both on 'C' (CAC, Figure 8c), the coordination is trigonal prismatic. (The letters represent the site configuration with lower S site, Mo site, upper S site.) The remaining two configurations are BAC (Figure 8d) and CAB (Figure 8e), which have octahedral coordination.

Folding a patterned continuous planar sheet of MoS₂ into an octahedron forms two more configurations. Folding this continuous sheet results in two configurations since the starting planar sheet of MoS₂ can have either trigonal prismatic or octahedral metal coordination and form octahedra maintaining the same bonding coordination. These octahedra possess T_d symmetry, i.e., they have less than full octahedral group symmetry since they lack inversion symmetry (or equivalently, they lack mirror planes through the edges). Figures 8f and 8g demonstrate how the positioning and number of S atoms change on adjacent faces of an octahedron with this scheme. In terms of the site notation defined above, the trigonal-prismatic-coordinated octahedron with T_d symmetry has BAB faces alternating with CAC faces (BAB/CAC, Figure 8f) and the octahedral-coordinated octahedron has BAC faces alternating with CAB faces (BAC/CAB, Figure 8g).

Independent of the six configurations, the number of Mo atoms (i.e., the number of A lattice sites) in an ideal octahedron is easily calculated to be $4N^2 + 2$ where N is the octahedral edge length in a -axis units (for $N = 12$ there are 578 Mo atoms). This assumes that Mo atoms are present at the vertices; subtract 6 if not. The number of B and C lattice sites in an ideal octahedron are $4N^2 + 4N$ and $4N^2 - 4N$, respectively. However, these numbers do not necessarily correspond to the numbers of S atoms associated with these sites because the three-dimensional geometry of the octahedron has less space for S atoms on the inside than on the outside of the Mo layer. For the octahedra with O_h symmetry, sulfur atoms below the B sites and adjacent to an edge are shared by adjacent faces of the octahedron, i.e., they lie in the mirror plane that passes through the edges. This is represented in Figures 8b and 8d by half and quarter shading for the inside S atoms and correspond to being shared by two or four faces, respectively. Also for configurations with O_h symmetry, there is room for additional S atoms in the space above the C sites. Again these atoms lie on the mirror

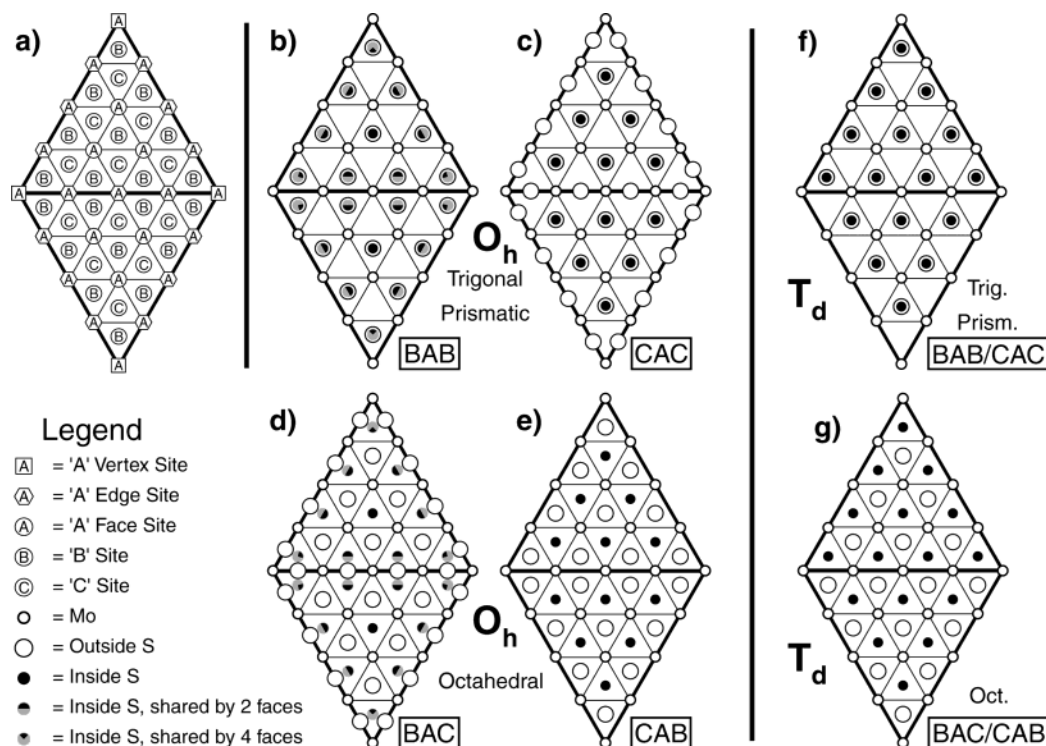


Figure 8. See legend in figure for symbol definitions. (a) Shows the site labeling convention used to discuss the atomic locations. Mo atoms will lie on the A sites and the S atoms will lie above and below the B or C sites. (b) BAB configuration with trigonal prismatic coordination and O_h symmetry. Note that the inner S atoms adjacent to the edges are shared by multiple Mo faces. (c) CAC configuration with trigonal prismatic coordination and O_h symmetry. Note that there is space for additional outer S atoms at the edges. (d) BAC configuration with octahedral coordination and O_h symmetry. At the edges, this has both inner S atoms shared and extra outer S atoms. (e) CAB configuration with octahedral coordination and O_h symmetry. (f) BAB/CAC configuration with trigonal prismatic coordination and T_d symmetry. (g) BAC/CAB configuration with octahedral coordination and T_d symmetry.

TABLE 1: For Configurations with O_h Symmetry, the Number of Sulfur Atoms Associated with the B and C Lattice Sites Depend on Whether the Sulfurs Are Located above or below the Mo Shell^a

location of S atom	number of S atoms for B site	number of S atoms for C site
inside Mo surface	$4N^2 - 8N + 6$ ($= 4(N - 1)^2 + 2$)	$4N^2 - 4N$
outside Mo surface	$4N^2 + 4N$	$4N^2 + 8N + 6$ ($= 4(N + 1)^2 + 2$)

^a The Mo shell is an octahedron with an edge length of N units and contains $4N^2 + 2$ Mo atoms. Note that the inside B site is equivalent to a sulfur octahedron with $(N - 1)$ edge length and the outside C site is equivalent to a sulfur octahedron with $(N + 1)$ edge length.

plane and appear in Figures 8c and 8d as outside S atoms on the edges of the faces. Table 1 lists the number of S atoms allowed for the B and C sites, depending on whether they are located on the inside or outside of the Mo surface for configurations with O_h symmetry. It is interesting to note that this adjustment to the number of S atoms is equivalent to forming complete octahedra of sulfur atoms inside or outside of the Mo octahedron. For the inside B sites, the sulfur octahedron has an edge length of $(N - 1)$ a -axis units, and for the outside C sites, the sulfur octahedron has an edge length of $(N + 1)$ units.

The various configurations can now be compared and Table 2 summarizes the coordination, symmetry, and number of sulfur atoms for the six configurations. The two configurations with O_h symmetry and trigonal prismatic coordination (BAB and CAC) cannot form nanooctahedra with the appropriate 2:1 S/Mo stoichiometry and therefore are not likely to exist without either the cluster possessing a net charge or significant deviations in

the Mo oxidation state. Configuration BAC (octahedral coordination, O_h symmetry) has the correct stoichiometry. Interestingly, the BAC configuration can be viewed as three nested octahedra (inner S, middle Mo, outer S) and as constructed has no bending strain. Closer examination of this structure, however, reveals that it suffers from nonideal sulfur bonding at the edges. The inner S edge atoms are coordinated to four Mo atoms whereas the outer S edge atoms are coordinated to only two Mo atoms rather than the normal three (Figure 9). Two-coordinate S bonding is reminiscent of edge sites on bulk MoS_2 and we feel will not be present in closed fullerene-like structures since the elimination of such dangling bonds is the driving force for creating the closed structures. The remaining three configurations (two T_d , one O_h symmetry) all have near ideal stoichiometry and bonding geometries. The one with the lowest free energy will be the best candidate for the nanooctahedra and depends on the free energy difference between the octahedral and trigonal prismatic bonding compared to the strain energy needed to close the structure. One must also keep in mind that these structures are formed at high temperatures where ordering of the thermodynamic stabilities of the various structures may be different than at room temperature.

If the bonding geometry about molybdenum in the nanooctahedra is trigonal prismatic, then the BAB/CAC structure with T_d symmetry is the only choice of the remaining three structures since the other two have octahedral coordination. If the bonding is octahedral, the CAB configuration (O_h symmetry) has significantly lower strain than BAC/CAB. With CAB, the Mo edge atoms actually have trigonal prismatic coordination with the S atoms; all the other Mo atoms on the faces are octahedrally coordinated (see Figure 10 inset). The trigonal prisms are oriented in such a way that allows more S atoms to

TABLE 2: Number of Sulfur Atoms for the Six Different Configurations of an Ideal Nanooctahedra with Edge Length Equal to N a -lattice Constants and Containing $4N^2+2$ Mo Atoms^a

config.	coord.	symmetry	no. inner S	no. outer S	total no. S	comments
BAB	trig. prism.	O_h	$4N^2-8N+6$	$4N^2+4N$	$8N^2-4N+6$	S poor
CAC	trig. prism.	O_h	$4N^2-4N$	$4N^2+8N+6$	$8N^2+4N+6$	S rich
BAC	octahedral	O_h	$4N^2-8N+6$	$4N^2+8N+6$	$8N^2+12$	S neutral improper S edge bonding
CAB	octahedral	O_h	$4N^2-4N$	$4N^2+4N$	$8N^2$	S neutral edge Mo are trig. prism. lower strain
BAB/CAC	trig. prism.	T_d	face I: $2N^2+2N$ face II: $2N^2-2N$ total in: $4N^2$	face I: $2N^2+2N$ face II: $2N^2-2N$ total out: $4N^2$	face I: $4N^2+4N$ face II: $4N^2-4N$ total: $8N^2$	total S neutral face I: S rich, face II: S poor higher strain
BAC/CAB	octahedral	T_d	face I: $2N^2+2N$ face II: $2N^2-2N$ total in: $4N^2$	face I: $2N^2-2N$ face II: $2N^2+2N$ total out: $4N^2$	face I: $4N^2$ face II: $4N^2$ total: $8N^2$	total S neutral faces S neutral higher strain

^a Of the six, only the CAB, BAB/CAC, and BAC/CAB configurations have proper stoichiometry and bonding saturations. Of these three, the CAB or the BAB/CAC configurations (bold) are the most likely to describe the actual nanooctahedra (see text).

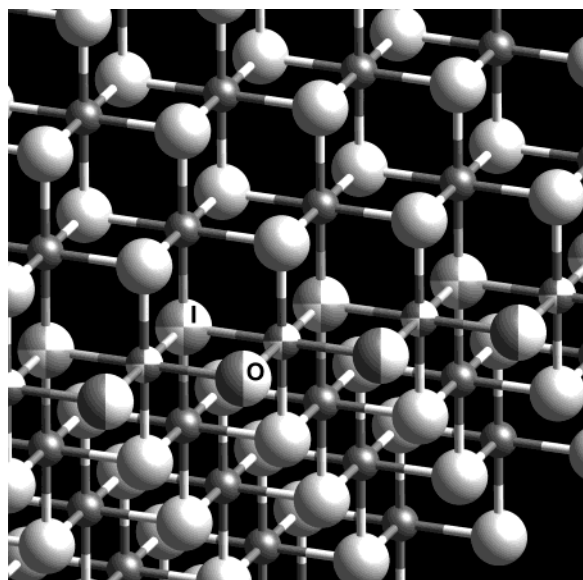


Figure 9. Close-up near the edge of a BAC octahedron. The inner-edge S atoms (quarter-patterned large spheres and one is labeled ‘I’ in the figure) are over-saturated with four bonds instead of the normal three. In contrast, the outer-edge S atoms (half-patterned large spheres and one is labeled ‘O’) are undersaturated with only two bonds. Edge Mo atoms are represented by the quarter-patterned small spheres, face Mo atoms are the small dark spheres, and face S atoms are the large light spheres. Because of this abnormal bonding, the BAC configuration is unlikely to occur.

be on the outside than on the inside of the Mo shell, i.e., the sulfur atoms are distributed to minimize crowding and its associated strain. In contrast, both T_d configurations have equal numbers of S atoms on the inside and outside of the Mo surface and crowding will be a problem. Furthermore, the edges of the CAB octahedron form “twin” boundaries for the octahedrally coordinated MoS_2 faces, and these boundaries have a natural dihedral angle of 141.06° . Comparing this angle to the 109.47° dihedral angle of an ideal octahedron reveals that this MoS_2 dihedral sheet must be bent 31.59° to form the octahedron. Again in contrast, the two T_d configurations start with planar sheets and therefore must be bent 70.53° to form the octahedron, again producing more strain. Figure 10 shows the natural 141.06° angle formed when two octahedrally coordinated sheets are joined at this twin boundary as well as the 109.47° and 180° reference angles. This type of “defect” may be critical in allowing the nanooctahedra to form and may also play an important role in providing curvature for other fullerene-like

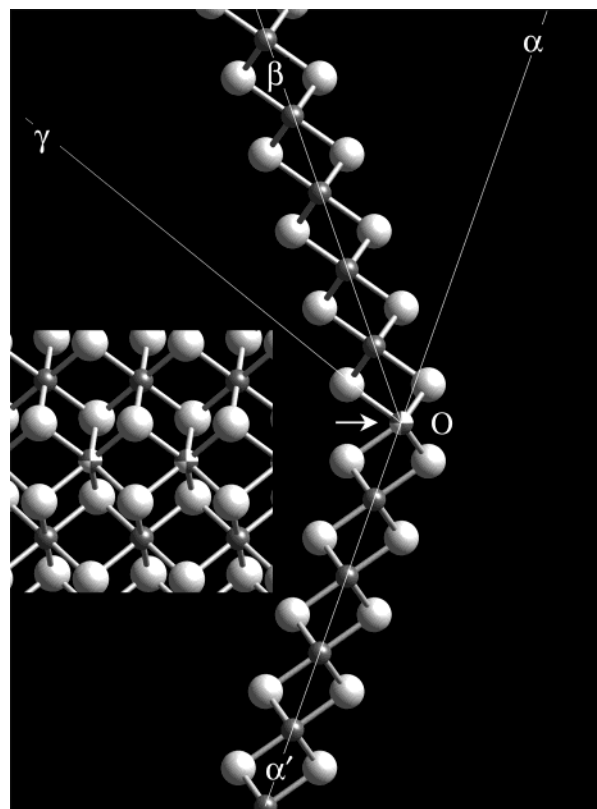


Figure 10. Side view of two octahedral-coordinated sheets joined along a line of Mo atoms with trigonal prismatic coordination (arrow and quarter-patterned sphere). The dihedral sheet so formed has an angle of 141.06° ($\angle\alpha'O\beta$). For comparison the 109.47° dihedral angle for an octahedron is shown ($\angle\alpha'O\gamma$) as well as the reference plane ($\alpha'\alpha$). The inset shows a close-up of the dihedral edge with its Mo atoms having trigonal prismatic coordination (small patterned spheres) with the S atoms (large light spheres), while all the other Mo atoms (small dark spheres) have octahedral coordination.

structures and nanotubes made from the layered transition metal chalcogenides.

Thus, the analysis presented here predicts that configurations CAB for octahedral coordination and BAB/CAC for trigonal prismatic bonding are the most favorable. An ab initio calculation is needed to determine which of these configurations has a lower total free energy (again keeping in mind the formation temperature) and to predict the actual structure for the nanooctahedra. Currently, there is no experimental evidence to support that the nanooctahedra have either of these configurations, and the Raman evidence is inconclusive in determining the bonding

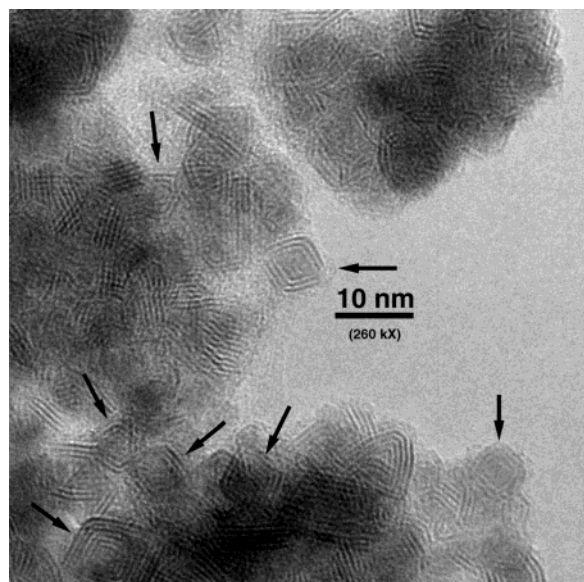


Figure 11. TEM micrograph of MoSe₂ soot shows an isolated nanooctahedron toward the center of the image (see arrow near scale bar). Several other nanooctahedra (other arrows) and polyhedral fullerene-like particles are also visible in the agglomerated material at the image periphery.

coordination due to the impurities in the samples. It may be possible to detect the symmetry of the nanooctahedra through high-resolution TEM measurements since the two symmetries differ by the arrangement of the sulfur atoms (see Table 2; in all cases, the Mo sublattice has O_h symmetry). Qualitatively, the TEM data appear consistent with O_h symmetry; however, this is inconclusive since calculations to model the TEM data are needed to ascertain the degree that the symmetry affects the TEM images. An additional complication is that all of the nanooctahedra found so far consist of multiple layers and even if each of the layers has T_d symmetry, the different layers may (and probably will) orient themselves to largely cancel out any asymmetry for the overall structure, i.e., a sulfur-poor face of one layer may align itself to be adjacent to a sulfur-rich face of another layer. Bulk layered dichalcogenide structures are known to have many stacking polytypes, due to the small energy differences in the mostly van der Waals interactions between the sheets, and so stacking polytypism may also be present in the nanooctahedra. This may also help explain why no single layer nanooctahedra have been observed since stacking interactions may help stabilize the structure. Final determination of the atomic structure for the nanooctahedra will require additional measurements.

Investigations into other Layered Chalcogenide Materials.

Given these results and the strong similarities among the layered transition metal chalcogenides, one must ask: Do similar IF structures exist in the other layered materials? We have started to answer this by applying the laser ablation synthesis technique to a number of layered materials. To date, MoSe₂, MoTe₂, WS₂, WSe₂, SnS₂, GaS, TaS₂, NbSe₂, and ReS₂ have been investigated. Of these compounds, we chose MoSe₂ first because of its similarity to MoS₂. Using a microwave plasma synthesis technique, Vollath et al.¹⁰ have investigated a similar range of materials (BN, MoS₂, WS₂, WSe₂, MoSe₂, SnS₂, and ZrSe₂).

Molybdenum Diselenide. TEM images of the soot produced by laser vaporization of the MoSe₂ target immediately showed that nanooctahedra of MoSe₂ were successfully produced. The types of projections found in the TEM images are identical to those from the MoS₂ soot (see Figure 11). This soot also

contained similar nested polyhedra, crystalline sheets, and spherically shaped particles as seen in the MoS₂ soot. Qualitatively, from an overall impression of the TEM images, it appears that MoSe₂ has a greater tendency than MoS₂ to form the nested polyhedral structures under these conditions. XRD of the soot revealed primarily Se and Mo crystalline phases with smaller signatures for the Mo₃Se₄ and MoSe₂ phases. The small MoSe₂ peak intensity is surprising since it is normally expected that some crystalline material from the target will be ejected during the vaporization process. The TEM images of this material show that there is a preponderance of layered fullerene-like material often coating the other particles in the soot. It is possible that MoSe₂ is especially well suited for PLV so that few bulk pieces are ejected from the target. The highly vaporized Mo and Se either condense to their elemental forms or recombine to form mostly MoSe₂ that then deposits layers on particles or forms nested irregular polyhedra and nanooctahedra. These highly curved MoSe₂ layers will produce a small XRD signal as compared to planar MoSe₂. Since MoSe₂ is isostructural to MoS₂, the Raman spectrum will show a corresponding signature for the metal–chalcogen bonding coordination, i.e., three modes are expected for the trigonal prismatic and two for the octahedral coordination. The Raman spectra taken from the MoSe₂ soot showed the three peaks associated with the trigonal prismatic coordination. Given that the XRD data indicated that bulk MoSe₂ was present in the soot, this is expected. As was the case for the MoS₂ soot, the question of which type of bonding coordination the MoSe₂ nanooctahedra have will not be answered until purified samples become available.

Bending Behavior. We propose that the widespread occurrence of highly curved surfaces in the TEM images of the soot indicates a strong potential for the material to form IFs. Thus, the materials tested here can be categorized according to this bending behavior, even if no definitive inorganic fullerene structures were identified. The following materials, listed from most promising to least, showed good bending behavior from the initial PLV experiments and deserve more intensive investigations to systematically determine whether any IF structures can be discovered: NbSe₂, WS₂, WSe₂, SnS₂, and TaS₂. Representative TEM images demonstrating this bending are shown in Figure 12. Several types of curved layering can be distinguished: irregular nested polyhedra, onions, and folding around existing particulates in the soot. In Figure 12b for SnS₂, there appears to be some indication of a superlattice similar to that reported by Hong et al.²⁹ Of particular interest is one of the NbSe₂ images given in Figure 13 where a candidate nanooctahedron has been identified. Additional evidence is required before we can definitively conclude the existence of nanooctahedra in NbSe₂. In the NbS₂ system, Schuffenhauer et al.¹⁶ have synthesized fullerene-like structures using a sulfidization process to form the nanoparticles, and so this material also deserves further investigation. The other materials investigated (GaS, ReS₂, and MoTe₂; again in order of most to least promising) did not show a high degree of bending behavior and appear unlikely to support the formation of IF structures. GaS represents a unique case because the hexagonal bulk crystal structure has a four-layer sandwich of S–Ga–Ga–S. If one considers the two Ga atoms as a single unit, the coordination could then be considered trigonal prismatic. The GaS system showed only crystalline platelet structures in the TEM images of the laser-ablated material. The fact that GaS evaporates congruently may account for the fact that laser vaporized material essentially reconstitutes nanoparticles of the starting material. Note that this effort is in its preliminary stages and

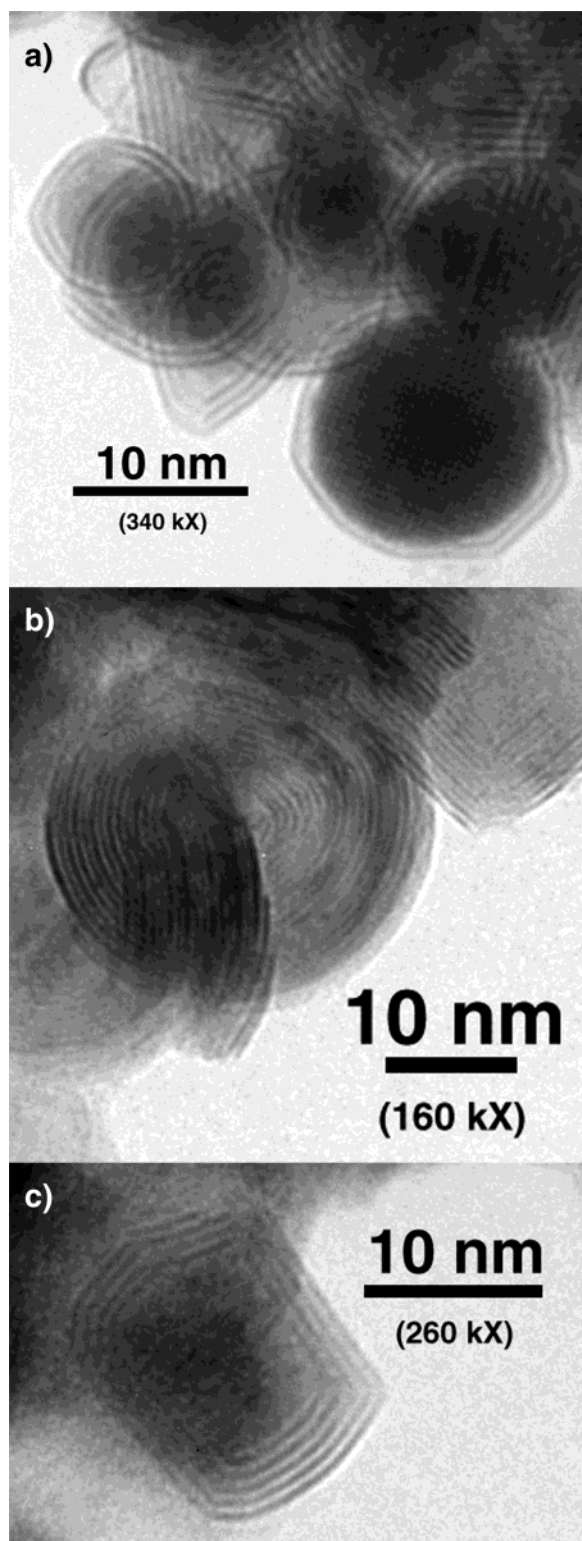


Figure 12. Series of TEM micrographs showing the typical contents of PLV soot for a few of the layered metal chalcogenides that showed some fullerene-like structures: (a) WS_2 , (b) SnS_2 , (c) TaS_2 .

the search for these unique structures has not been exhaustive. It is quite possible that any of these materials are capable of producing IFs with suitable synthesis parameters. Two illustrations that the synthesis route influences the final structures are evident in the works of Coleman et al.,¹⁵ where ReS_2 produced by the sulfidization of ReO_2 with H_2S formed layered onion and tube structures, and Brorson et al.,¹⁴ where ReS_2 nanotubes were formed using carbon nanotubes as a template.

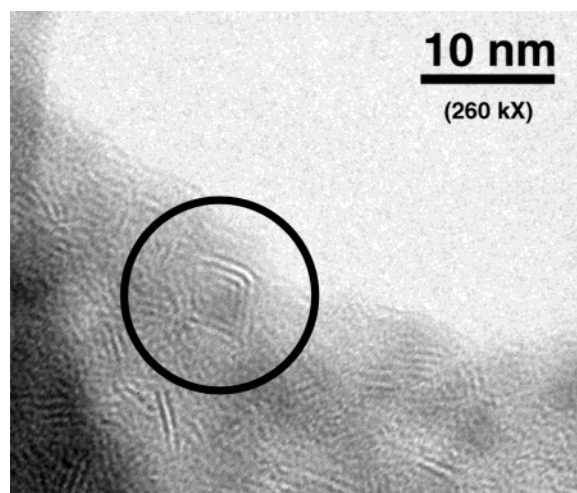


Figure 13. Candidate nanooctahedron in NbSe_2 PLV soot is pictured in the circle of this TEM micrograph. There was insufficient data to confidently confirm that this and a few other observed structures have the nanooctahedra structure.

The sensitivity to the synthesis method is further exemplified in comparing this work with Vollath et al.¹⁰ where there is significant overlap in the materials studied (MoS_2 , MoSe_2 , WS_2 , WSe_2 , and SnS_2). Although Vollath et al. did not find any nanooctahedra in any of the materials that they investigated, there were similarities in the soot produced. Nanocrystalline particles were common for most of the investigated materials in both studies, and under certain conditions, Vollath et al. were able to produce fullerene-like onions. For these common materials, it seems that PLV is better adapted to produce fullerene-like structures such as onions and nanooctahedra. Another interesting difference is that the microwave technique produced mostly amorphous structures for WSe_2 while PLV produced several types of fullerene-like structures and is categorized as being very promising for forming the nanooctahedra. The results of these experiments provide valuable clues to the critical processes that allow for the formation of fullerene-like structures. While onion structures can be formed using relatively slow processes, the nanooctahedra may require much faster and higher temperature processes, such as those occurring in the PLV method.

Conclusions

We have presented convincing arguments that we have produced nanooctahedra of MoS_2 and MoSe_2 in distinct sizes. Because of their high symmetry and distinct sizes, these nanooctahedra are a new benchmark in the synthesis of analogues to the carbon fullerenes. Many unresolved questions still exist: what is the exact structure of the nanooctahedra?; are the nanooctahedra hollow?; if not what is the composition of the core of the nanocluster?; what is the atomic arrangement at the vertices?; what is the mechanism of the formation of the nanooctahedra? There are also the practical issues of yield, purification, and separation. Several other layered metal chalcogenides were investigated and showed clear indications of fullerene-like structures. Clearly, we expect unique physical, chemical, and optoelectronic properties from these and other yet-to-be-discovered fullerene-like structures composed of elements other than carbon.

Acknowledgment. The authors acknowledge the Department of Energy's Office of Science — Materials Sciences and Engineering Division and the DDRD Program at NREL, both

under DOE contract number DE-AC36-99G010337. B.A.P. also acknowledges NSF grant number DMR 0107429.

References and Notes

- (1) Kroto, H. W.; Heath, J. R.; O'Brien, S. C.; Curl, R. F.; Smalley, R. E. *Nature* **1985**, *318*, 162.
- (2) Iijima, S. *Nature* **1991**, *354*, 56.
- (3) *Fullerenes*; Kadish, K. M., Ruoff, R. S., Eds.; The Electrochemical Society: Pennington, NJ, 1997; Vol. 4.
- (4) Koruga, D.; Hameroff, S.; Withers, J.; Loufty, R.; Sundareshan, M. *Fullerene C₆₀*; North-Holland: Amsterdam, 1993.
- (5) *Carbon Nanotubes Synthesis, Structure, Properties and Applications*; Dresselhaus, M. S., Dresselhaus, G., Avouris, Ph., Eds.; Springer-Verlag: Berlin, 2001; Vol. 80.
- (6) Banhart, F.; Zwanger, M.; Muhr, H.-J. *Chem. Phys. Lett.* **1994**, *231*, 98.
- (7) Chopra, N. G.; Luyken, R. J.; Cherrey, K.; Crespi, V. H.; Cohen, M. L.; Louie, S. G.; Zettl, A. *Science* **1995**, *269*, 966.
- (8) Margulis, L.; Salitra, G.; Tenne, R.; Talianker, M. *Nature* **1993**, *365*, 113.
- (9) Tenne, R. *Adv. Mater.* **1995**, *7*, 965.
- (10) Vollath, D.; Szabo, D. V. *Acta Mater.* **2000**, *48*, 953.
- (11) Sen, R.; Govindaraj, A.; Suenaga, K.; Suzuki, S.; Kataura, H.; Iijima, S.; Achiba, Y. *Chem. Phys. Lett.* **2001**, *340*, 242.
- (12) Sano, N.; Wang, H. L.; Chhowalla, M.; Alexandrou, I.; Amaratunga, G. A. J.; Naito, M.; Kanki, T. *Chem. Phys. Lett.* **2003**, *368*, 331.
- (13) Parilla, P. A.; Dillon, A. C.; Jones, K. M.; Riker, G.; Schulz, D. L.; Ginley, D. S.; Heben, M. J. *Nature* **1999**, *397*, 114.
- (14) Brorson, M.; Hansen, T. W.; Jacobsen, C. J. H. *J. Am. Chem. Soc.* **2002**, *124*, 11582.
- (15) Coleman, K. S.; Sloan, J.; Hanson, N. A.; Brown, G.; Clancy, G. P.; Terrones, M.; Terrones, H.; Green, M. L. H. *J. Am. Chem. Soc.* **2002**, *124*, 11580.
- (16) Schuffenhauer, C.; Popovitz-Biro, R.; Tenne, R. *J. Mater. Chem.* **2002**, *12*, 1587.
- (17) Stephan, O.; Bando, Y.; Loiseau, A.; Willaime, F.; Shramchenko, N.; Tamiya, T.; Sato, T. *Appl. Phys. A* **1998**, *67*, 107.
- (18) Golberg, D.; Bando, Y.; Stephan, O.; Kurashima, K. *Appl. Phys. Lett.* **1998**, *73*, 2441.
- (19) Wilson, J. A.; Yoffe, A. D. *Adv. Phys.* **1969**, *18*, 193.
- (20) Yang, D.; Sandoval, S. J.; Divigalpitiya, W. M. R.; Irwin, J. C.; Frindt, R. F. *Phys. Rev. B* **1991**, *43*, 12053.
- (21) Feldman, Y.; Wasserman, E.; Srolovitz, D. J.; Tenne, R. *Science* **1995**, *267*, 222.
- (22) Seifert, G.; Terrones, H.; Terrones, M.; Jungnickel, G.; Frauenheim, T. *Phys. Rev. Lett.* **2000**, *85*, 146.
- (23) Goldstein, H. *Classical Mechanics*; Addison-Wesley: Reading, MA, 1950; p 109.
- (24) Seifert, G.; Kohler, T.; Tenne, R. *J. Phys. Chem. B* **2002**, *106*, 2497.
- (25) Huisman, R.; Jonge, R. D.; Haas, C.; Jellinek, F. *J. Solid State Chem.* **1971**, *3*, 56.
- (26) Mills, K. *Thermodynamic Data for Inorganic Sulphides, Selenides, and Tellurides*; Butterworth & Co. Ltd.: London, 1974.
- (27) Exfoliated MoS₂ is typically formed by intercalation of an alkali metal into bulk MoS₂ and subsequent reaction with water or alcohol. Although the subsequent alkali-hydroxide can be largely removed from the exfoliated material, it is not clear whether any alkali material remains, and if so, what role it may have in the trigonal prismatic to octahedral coordination transformation.
- (28) Sandoval, S. J.; Yang, D.; Frindt, R. F.; Irwin, J. C. *Phys. Rev. B* **1991**, *44*, 3955.
- (29) Hong, S. Y.; Popovitz-Biro, R.; Prior, Y.; Tenne, R. *J. Am. Chem. Soc.* **2003**, *125*, 10470.